A simulation environment for validating ultrasonic blood flow and vessel wall imaging based on fluid-structure interaction simulations: ultrasonic assessment of arterial distension and wall shear rate

5

Authors: Abigail Swillens[1], Joris Degroote[2], Jan Vierendeels[2], Lasse Lovstakken[3], Patrick Segers[1]

[1]Institute Biomedical Technology, Ghent University, De Pintelaan 185, 9000 Gent

10   [2]Department of flow, heat and combustion mechanics, Ghent University, Sint-

Pietersnieuwstraat 41 ,9000 Gent

[3]Norwegian University of Science and Technology, Department of Circulation and Medical

Imaging, Olav Kyrres gt. 9, 7489 Trondheim, Norway

15   Correspondence:

Abigail Swillens

Ghent University

IBiTech-bioMMeda

De Pintelaan185

20   9000-Gent, Belgium

abigail.swillens@ugent.be

Tel: +32 9 332 33 79

Fax: +32 9 332 41 59

25

Abstract

Purpose: Ultrasound is a commonly used vascular imaging tool when screening for patients at high cardiovascular risk. However, current blood flow and vessel wall imaging methods are hampered by several limitations. When optimizing and developing new ultrasound modalities, proper validation is required before clinical implementation. Therefore, we present a simulation environment integrating ultrasound (US) and fluid-structure interaction (FSI) simulations, allowing construction of synthetic ultrasound images based on physiologically realistic behavior of an artery. To demonstrate the potential of our model for vascular ultrasound research, we studied clinically relevant imaging modalities of arterial function related to both vessel wall deformation and arterial hemodynamics: arterial distension (related to arterial stiffness) and wall shear rate (related to the development of atherosclerosis) imaging.

Methods: An in-house code ("Tango") was developed to strongly couple the flow solver Fluent and structural solver Abaqus using an Interface Quasi-Newton technique. Field II was used to model realistic transducer and scan settings. The input to the FSI-US model is a scatterer phantom on which the US-waves reflect, with the scatterer displacement derived from the FSI flow and displacement fields. We applied our simulation tool to a 3D straight tube, representative of the common carotid artery (length 5cm, inner and outer radius: 3 and 4 mm). A mass flow inlet boundary condition, based on flow measured in a healthy subject, was applied. A downstream pressure condition, based on a non-invasively measured pressure waveform, was chosen and scaled to simulate three different degrees of arterial distension (1%, 4%, 9%). The RF-data from the FSI-US coupling were further processed for arterial wall and flow imaging. Using an available wall tracking algorithm, arterial distensibility was assessed. Using an autocorrelation estimator,

blood velocity and shear rate were obtained along a scanline. ***Results:*** We obtained very good agreement between the flow and distension as obtained from the FSI-US model and the reference FSI values. The wall application showed a high sensitivity of distension measurements to the measurement location, previously reported based on in vivo data. Interestingly, the model indicated strong reflections between tissue transitions can potentially cloud a correct measurement. The flow imaging application demonstrated maximum shear rate was underestimated for a relevant simulation setup. Moreover, given the difficulty of measuring near-wall velocities with ultrasound, maximal shear rate was obtained at a distance from the wall (0.812 mm for the anterior and 0.689 mm for the posterior side (9%-case)). However, ultrasound shear rates correlated well with the FSI ground truth for all distension degrees, suggesting correction of the severe underestimation by ultrasound might be feasible in certain flow conditions. ***Conclusions:*** We demonstrated a simulation environment to validate and develop ultrasonic vascular imaging. An elaborate technique to integrate FSI and Field II ultrasound simulations was presented. This multiphysics simulation tool was applied to two imaging applications where distensible ultrasound phantoms are indispensable: wall distension and shear rate measurement. Results showed our method to couple fluid-structure interaction and ultrasound simulations provides realistic RF signals from the tissue and the blood pool.

Keywords: multiphysics, ultrasound, fluid-structure interaction, vessel distension, wall shear rate

3

Introduction

At present, ultrasonic echography is still the preferred method for clinical screening of atherosclerosis in large, superficial arteries. In particular, the carotid artery is often investigated in clinical protocols since the artery directly supplies blood to the brain and the location is prone to development of atherosclerosis. Moreover, as the carotid artery is a large elastic vessel, measuring its stiffness might indirectly provide information on aortic stiffening. Hence, its screening may identify subjects at risk of cardiovascular disease in general, and stroke in particular. However, current ultrasound modalities have their limitations in this setting. Most commonly used clinical blood flow imaging modalities are still limited to 1D measurements since only the velocity component in the direction of the ultrasound beam is visualized. This is particularly a disadvantage for complex velocity fields as may occur in the vicinity of the carotid bulb, where zones of blood recirculation and swirling flow patterns may arise[1]. Other imaging modalities aim to assess arterial stiffness, but here the current methods are also hampered. A common application is measuring tissue velocities using Doppler based methods, which is limited to 1D visualization as well. Often, tissue velocities are further integrated to assess vessel distension[2]. However, vessel kinematics rather than vessel mechanics is hence assessed.

With the rapid evolution in ultrasound imaging technology and computer processing power, it has become feasible to design better imaging modalities. A practical problem is however the validation and optimization of these imaging modalities. Especially for complex settings as the carotid artery, which shows complex flow patterns and a highly deformable elastic wall, new and optimized ultrasound modalities (pulse firing sequences, beam-forming, processing of radio-frequency (RF) ultrasound data) aiming for improved visualization would require thorough validation.

In recent work[3], we developed a computer simulation tool which integrated computational fluid dynamics (CFD) with ultrasound simulation (US) software (Field II[4, 5]), providing a flexible tool for the validation and development of ultrasound blood flow modalities in the presence of complex flow. In the simulation environment, the ultrasonic echoes are simulated by modeling blood as a random point scatterer distribution on which the ultrasound waves reflect. The scatterer positions are updated using the CFD-velocity fields interpolated in space and time. We used this tool to construct a patient-specific 3D ultrasound phantom of the carotid artery and we assessed the performance of 1D flow imaging methods like pulsed wave Doppler and color flow imaging, demonstrating its inability to portray complex flow patterns[3]. We further compared the performance of two major research lines in 2D velocity estimators: crossed-beam vector Doppler and speckle tracking, demonstrating that speckle tracking would probably make most chance to be practically applicable [6].

An important limitation of our work, however, was the absence of the moving vessel wall in our model, which influences flow visualization through the motion of the boundaries of the fluid domain, as well as via ultrasound echoes generated by the vessel wall. Fluid-structure interaction (FSI) simulations allow for the coupled computation of blood flow and arterial wall mechanics. It is therefore a natural extension of our work to seed scatterers also in the vessel wall, and to use FSI-simulations to calculate scatterer positions in both the blood flow and vessel wall. Although the basic principle behind this extension is logical and straightforward, the practical implementation is not. A first challenge is the grid formulation used in FSI-simulations, where both the fluid and structural part are described with nodal grid positions changing with time, which challenges the scatterer position assessment. Further, the creation of a vessel wall phantom also poses specific challenges. In

5

contrast to blood scatterers which move in and out of the computational domain, tissue scatterers are fixed to the tissue. The complex composition and layering of the vessel wall also requires flexibility in adapting scattering properties in localized regions. Implementing the layered structure in the scatterer phantom imposes

130   additional requirements on the mesh elements used to solve the structural problem. Furthermore, the transition between the vessel wall and surrounding tissue/blood creates strong specular reflections, which should be appropriately mimicked in the ultrasound software.

The aim of this paper is two-fold. In a first section, we elaborate on our methodology

135   based on a 3D FSI-simulation of blood flow and wave propagation in a 3-layered tube, representative of the common carotid artery. Scatterer phantoms of both the blood flow and arterial wall are generated and hence a virtual echographic phantom of a straight arterial segment is obtained. In a second section, the potential of the model is illustrated via two applications on currently used ultrasound modalities in vascular

140   research, one related to measuring distension of the arterial wall and one related to assessing the wall shear stress exerted by the blood flow on the arterial wall.

As a first application, the ultrasonic measurement of vessel distension will be investigated, which is often used to measure arterial stiffness. We will use the RF-data resulting from scatterers in the arterial wall to assess the performance of a

145   previously used [7] vessel wall-tracking algorithm based on a modified autocorrelation velocity estimation algorithm[2]. In particular, the sensitivity of these wall-tracking algorithms to the measuring position in the arterial wall will be demonstrated, where we anticipate a decrease in measured diameter distension from the blood-lumen interface towards the adventitia, as we have previously reported in vivo[7]. In a second

150   application, we will study to what extent it is possible to measure velocity and shear

rate profiles using Doppler-based measurements along one scanline. The shear rate relates to the tangential force exerted by the blood on the endothelial cells, which line the lumen of the blood vessel. Low or oscillating shear stress has been shown to promote the development of atherosclerosis, and is hence a clinically relevant

155 hemodynamic parameter when screening for patients at high cardiovascular risk[8]. As earlier described by Brands et al.[9], shear rate profiles can be derived from flow velocity profiles measured with ultrasound. However, due to difficulties in measuring the low velocities in the vicinity of the moving wall, the maximal shear rate is measured at a certain distance from the wall, while the actual maximal shear rate

160 might be differing from this position and in magnitude. To the best of our knowledge, the relationship between ground-truth and ultrasound-derived shear rate has never been studied in detail. As the magnitude of the wall motion might have an effect on this relation, we have performed three simulations with various degrees of arterial distension.

165

170

Methods

A. Simulating Fluid-Structure interaction (FSI)

175   FSI-simulations were performed in a partitioned way, computing the flow and structural equations with a separate flow and structural solver. An in-house code 'Tango' was used to couple the flow solver Fluent (Ansys, Canonsburg, PA, USA) and the structural solver Abaqus (Simulia,Inc., Providence, RI, USA). In particular, Dirichlet-Neumann partitioning was used, which means the flow problem is solved for

180   a given displacement, and the structural problem is solved for a stress boundary condition applied on the wet side of the structure. For each timestep, coupling iterations were performed between the flow and structural solver, and the transfer of information was limited to the fluid-structure interface: a face stress transfer from fluid to structural domain and a displacement transfer from structural to fluid domain.

185   However, vascular FSI-problems are often strongly coupled problems due to the compliant vessel walls and the similar fluid and structural densities. Hence, a weak coupling, i.e. directly transferring the stresses and displacements may lead to numerical instabilities [10, 11]. To enhance convergence of the coupling iterations, an Interface Quasi-Newton method was used [12, 13]. This technique replaces the complex

190   fluid or solid solver on the interface by approaching the Jacobian of the solver on the interface. Further, an Arbitrary Lagrangian Eulerian (ALE) method was used to match the different grid formulations for the fluid and structural domain. The fluid domain is often described in the Eulerian way, which considers motion from a fixed point. The Lagrangian formulation is the intuitive way of describing the structural domain, and

195   considers motion from a point moving with the material. In the ALE method, the flow equations are written in an arbitrary Lagrangian-Eulerian formulation and are solved

on a deforming mesh. The fluid grid deforms in an arbitrary way, independent from the flow velocity, and its boundaries follow the structural domain's deformation. The structural problem is formulated in the Lagrangian manner.

200   A straight elastic tube with inner radius 3 mm, outer radius 4 mm, and length 5 cm was simulated. The vessel wall was modeled using a linearized elastic material model with a Young modulus of 250 kPa, Poisson modulus of 0.49, and density 1200 kg/m^3. The linearization was performed with respect to a reference pressure and inner radius of respectively 10 mmHg and 3mm. Circumferential and longitudinal

205   movement of the tube was prevented. Blood was modeled as a Newtonian liquid with a viscosity of 3.5 mPas and a density of 1050 kg/m^3. A velocity profile was measured in the common carotid artery of a healthy volunteer using ultrasonic pulsed wave Doppler (12L linear array vascular probe, GE Medical Systems, Milwaukee, WI, USA) and was applied as a mass flow inlet condition to increase stability during the

210   coupling iterations. The outlet boundary condition was a non-invasively measured pressure waveform, scaled with a pulse pressure of 40 mmHg, representative of a healthy hemodynamical condition. This pressure condition resulted in an arterial distension $\Delta D/D$ ($\Delta D = D_{max} - D_{min}$ and $D = D_{min}$) of 9%. To obtain additional datasets with lower degree of distension, we ran simulations using the same pressure waveform,

215   but with an amplitude scaled to pulse pressures of 20 and 4 mmHg or arterial distensions of 4% and 1%. The fluid-structure interface was modeled as a no-slip boundary.

The flow solver Fluent uses a finite volume method, with PISO pressure-velocity coupling and first order time accuracy. First order pressure discretization and second

220   order upwind for momentum were applied. The fluid mesh consisted of 34400 triangular prisms and was adapted to the position of the fluid-structure interface with

a spring analogy. Abaqus is a finite element structural solver which uses Hilber-Hughes-Taylor[14] implicit time integration and takes into account the geometric non-linearities due to large deformations. The structural domain was composed of 720 quadratic continuum hexahedrons (20 nodes) and numerical damping of high-frequency errors was increased ($\alpha=-0.3$) to eliminate spurious oscillations due to the different time discretizations in Fluent and Abaqus. Hexahedral elements were used to allow layered modeling of the vessel wall. A non-conforming mesh existed on the interface requiring appropriate interpolation of the transfer variables. The cardiac cycle of 1s was divided into timesteps of 5 ms and 2 cycles were computed to obtain results independent of transient effects. The Womersley number was 4.12; the peak Reynolds number was 845 (1 %-case). The coupling algorithm was executed on one core, the flow solver on six cores and the structural solver on six cores of a dedicated machine with two Intel Xeon 5355 quad-core processors (2.66GHz).

B. Simulating ultrasound

The RF-signals from the vessel wall and blood were simulated using the Field II software created by Jensen et al[4, 5]. This simulation software allows modeling arbitrary ultrasound transducers and realistic image scan sequencing. The approach is limited to linear wave propagation and is based on the spatial impulse response estimation as described by Tupholme [15] and Stepanishen [16]. Using linear system theory, the ultrasound field is determined based on the ultrasonic excitation pulse, the temporal impulse responses of the transmitting and receiving transducers, and the spatial impulse response at a given point. For further details on the software background, we refer to [4, 5]. Field II models tissue as a collection of random point scatterers. The required scatterer density is related to the imaging system resolution, with 10 scatterers per resolution cell assuring Gaussian distributed RF-signals [17]. The

scattering strength is modeled using a normal distribution of scattering amplitudes with mean and standard deviation varying according to the tissue properties. To appropriately mimic specular reflections, scatterers with high mean amplitude are positioned in a regular fashion at the tissue transitions. Dynamic objects are achieved by moving the point scatterers during simulation. Each ultrasound beam is simulated individually, and it is therefore possible to update the position of moving scatterers between beam acquisitions.

B1. Integrating FSI and ultrasound: creating a fluid scatterer phantom

In [3], we described a method to generate scatterers during Field II simulations based on CFD-calculations with rigid walls. 3D spatial interpolation was performed to transform the CFD velocity vectors to the random scatterer cloud, and temporal interpolation of the CFD velocities was required due to the large disparity in the ultrasound and CFD timescales (63 μs versus 5 ms for the simulated color flow imaging application).

For distensible fluid geometries, straightforward linear temporal interpolation of the velocity fields is however not possible. This is illustrated in fig. 1-A, if one considers the position of the red point at time point $T_{FSI,1}$ of the FSI-calculation and the same absolute position of this point at the next FSI timestep $T_{FSI,2}$. In case of a decreasing fluid volume, this point ends up outside the fluid volume at $T_{FSI,2}$ (white point in fig.1-A). In case of increasing fluid volume, the point ends up further from the vessel wall at $T_{FSI,2}$ compared to $T_{FSI,1}$ (yellow point in fig.1-A). Hence, temporal interpolation between the same absolute positions at different FSI-timesteps is incorrect. Complex mathematical methods exist to derive velocity fields for changing fluid domains at timesteps intermediate to the chosen FSI-timesteps. This, however, would be an

impractical approach due to high computational times [18, 19]. We therefore followed an approach outlined below, which allowed us assessing scatterer velocities as illustrated in the flowchart of fig. 1-B.

The scatterer displacement will be approximated by updating scatterer velocities for each FSI-timestep. A first problem arises from the fact that when deriving scatterer velocities using the *current* situation at FSI-frame $T_{FSI,1}$, the scatterer positions at subsequent ultrasound simulation timesteps will not follow the wall motion. This is illustrated for the red point in fig. 1-A, with corresponding velocity vector V at $T_{FSI,1}$. For increasing volumes, the red scatterer would be propagated in a horizontal manner according to the vector V, and a void would arise near the wall. In case of decreasing volumes, the red scatterer would end up outside the fluid volume due to its horizontal propagation. In order to follow the wall motion, the situation at the *next* FSI-timestep $T_{FSI,2}$ should be considered when updating the scatterer velocity at $T_{FSI,1}$. As illustrated in fig. 1-A, the red scatterer has a velocity vector V at $T_{FSI,2}$ which indicates the correct wall motion. The velocity vectors at $T_{FSI,2}$ will therefore be applied for the ultrasound simulation timesteps $\geq T_{FSI,1}$ and $< T_{FSI,2}$.

Now we know *when* to extract the scatterer velocities, the question remains *where* to extract the scatterer velocity vector from the velocity field at $T_{FSI,2}$. As was previously explained, absolute positions at different FSI-timesteps can not be compared. Consequently, one cannot extract the velocity vector at $T_{FSI,2}$ at the same location the scatterer finds oneself at $T_{FSI,1}$. A suitable location can be found, keeping in mind the scatterer displacement between FSI-timesteps is influenced by both the flow and structural movement. If a flow scatterer were solely displaced due to the structural movement, one can assume that its relative position in the blood vessel is conserved. To find the same relative location of a scatterer at $T_{FSI,2}$, the scatterer location at

$T_{FSI,1}$ is *mapped* onto its new location at $T_{FSI,2}$ using the deformation of the fluid grid between $T_{FSI,1}$ and $T_{FSI,2}$. This is also illustrated in fig. 1-A. This is possible because of the ALE grid formulation and since remeshing is unnecessary due to the relatively small volume changes between FSI timesteps (typical for vascular FSI-applications). For this purpose, the fluid grid deformation known in the nodal grid points is interpolated to the random points using the same Matlab procedure as described in [3].

Once the mapped scatterer location at $T_{FSI,2}$ is known, the velocity vector of the scatterer can be obtained with 3D spatial interpolation[3]. Subsequently, the new scatterer position $\vec{X}_{t_n}$ at t_n ($T_{FSI,1} < t_n \leq T_{FSI,2}$) can be calculated as:

$$\vec{X}_{t_n} = \vec{X}_{t_{n-1}} + \vec{v}_{T_{FSI,2}}(\vec{X}_{T_{FSI,1},mapped}) \cdot \Delta T$$

With $\vec{X}_{t_{n-1}}$ the scatterer position at the previous timestep t_{n-1}, ΔT the timestep between t_{n-1} and t_n, and $\vec{v}_{T_{FSI,2}}(\vec{X}_{T_{FSI,1},mapped})$ the velocity vector at $T_{FSI,2}$ at the location found by mapping the scatterer position $\vec{X}_{T_{FSI,1}}$ on the next FSI-timestep $T_{FSI,2}$. A complete overview of the procedure can be found in fig. 1-B.

B2. Integrating FSI and ultrasound: creating a structure phantom

The structure phantom generation is less complex because of the Lagrangian grid formulation. The grid displacement corresponds with the material displacement and hence also with the scatterer displacement. However, the vessel wall needs more refined scatterer generation due to its complex composition, with flexibility of defining different scattering properties in different vessel regions. Therefore, point scatterers are generated in each hexahedron of the structural mesh. This way, scattering

characteristics can be changed at very localized regions of the wall. In particular, the mesh was divided into 3 layers of hexahedrons, with scatterer properties easily modifiable for each layer. This represents to some extent the intima, media and adventitia of an artery, although we assumed equal thickness of each layer, while this is not the case in vivo. For each hexahedron of the mesh, a surrounding box was used to randomly generate scatterers, with points outside the bounding box being deleted, as illustrated in fig. 2-A. Displacement vectors were obtained by subtracting the grid position of $T_{FSI,1}$ from $T_{FSI,2}$ and assigning them to the scatterers by weighted averaging. Besides these random scatterers, the vessel wall also causes specular reflections at the transition regions between different tissue types (i.e. tissue/vessel wall and vessel wall/blood). Specular reflections can not be simulated in Field II but can be mimicked by positioning scatterers in a regular fashion at the wet and dry boundary of the structure, as illustrated in fig. 2-A. More specifically, for each hexahedron in the intima or adventitia layer, the side adjacent to a different tissue type was determined and scatterers were placed at fixed distances. These mimicked specular reflections had a higher intensity than the scattering from the random tissue and blood scatterers. An overview of the different scattering properties attributed to the different tissues can be found in table 1.

C. Ultrasonic imaging setup

Ultrasound applications for both flow and vessel wall imaging were investigated to validate and apply the new simulation tools. Wall shear stress imaging as described by [9, 20] and distension measurements [2] were chosen since distensible vessel phantoms are important for their analysis. For both applications, a linear array transducer with appropriate centre frequency and excitation was implemented. Each transducer element was divided into four smaller rectangular mathematical elements

so that the backscattered signal from each point scatterer was simulated with sufficient accuracy. The focal depth position was set at 2 cm, and a dynamic focus and expanding aperture was used on receive to retain constant imaging properties throughout depth. To reduce beam sidelobes, apodization was applied (=amplitude weighting of the receiving transducer elements). A complete overview of the simulation parameters can be found in table 1. Both methods were based on ultrasonic velocity estimation of respectively blood and tissue as described below.

C1. Vessel wall imaging application: measurement of vessel distension

When measuring vessel distension, ultrasound signals are emitted perpendicular to the vessel wall. Vessel wall motion was tracked by integrating wall velocities: $z[t+\Delta t]=z[t]+v[t]\Delta t$, with $z[t]$ the position in the vessel wall, $v[t]$ as estimated by ultrasound (modified autocorrelation approach[2]), and Δt the velocity resolution corresponding to the packet size times the pulse repetition period (3·1/1000). Only the RF-data of the arterial wall were processed for this application, hence neglecting a potential effect of the flow motion on the wall velocity estimator. Compared to the flow imaging application, an imaging setup with much higher resolution was required (i.e. shorter pulselength and higher frequency). The 12L linear array probe (GE Medical Systems, Milwaukee, WI, USA), as used in the applied distension software [2,7], was modeled with a 1.5 period sinusoidal pulse excitation of 8 MHz centre frequency. Due to the lower velocity range of tissue compared to blood, a lower PRF of 1 kHz was applied. Details of the ultrasound set-up are provided in Table 1.

C2. Flow imaging application: measurement of wall shear rate

For this application, the tube phantom was angled 70 degrees with respect to the ultrasound beam (=axial) direction, which is of the same order of magnitude as when

measuring carotid blood flow in vivo. Velocity profiles in the axial direction were obtained using the autocorrelation algorithm described for ultrasound applications by Kasai et al [21], as most often used in color flow imaging. An ensemble of ultrasonic pulses is fired along the arterial cross-section and the phase-shift between the backscattered ultrasonic waves was estimated. The axial velocity v_z was calculated

according to: $v_z = \dfrac{cPRF}{4\pi f_0} \arctan(\dfrac{\text{Im}(\hat{R}(1))}{\text{Re}(\hat{R}(1))})$, with PRF (=pulse repetition frequency) the frequency of emitting ultrasound beams, f_0 the centre frequency of the ultrasound pulse and $\hat{R}(1)$ the estimated autocorrelation function at lag 1. The Doppler signal from blood is completely defined by the autocorrelation function since it can be described by a complex Gaussian proces, and hence $R(1)$ can be approximated with

N-1 pairs of complex samples Z: $\hat{R}(1) = \dfrac{1}{N-1}\sum_{i=1}^{N-1} Z(i-1)Z*(i)$.

Note that only the RF-signal from the blood was used to estimate flow velocities. Hence, no clutter filter was applied to the data. A 4-period sinusoidal excitation pulse with 5 MHz centre frequency was chosen. Velocity profiles halfway the tube were obtained using a packet of 64 (=N) pulses emitted with a PRF of 8 kHz, resulting in 120 frames for the complete cardiac cycle. As described by [20], the two-dimensional distribution of angle-corrected velocities was smoothed by a 2D median filter (2 pulselengths in depth and 3 cardiac frames) to remove occasional extreme velocity values. A sliding window averaging filter was used to remove further fluctuations. In the results, all displayed velocities are angle-corrected velocities and thus represent velocities along the axis of the tube.

Results

For all three simulated cases, converged FSI simulations of two cardiac cycles were obtained within 12 hr. These FSI-datasets provided reference data on the deformation of the vessel wall and on the flow field and derived wall shear rate. RF-data of the complete cardiac cycle were obtained from the ultrasound simulations within 1.7 hr and 16 hr. for respectively the fluid and structural part on 3.4 GHz Intel Pentium IV processors.

A.Vessel wall imaging application: measurement of vessel distension

RF ultrasound data for the wall were generated from the FSI-US coupling procedure, and are displayed as an M-Mode image in fig. 3-A. Using the distension software of Rabben et al [2], the motion of the anterior and posterior intima-lumen transitions was tracked ("inner wall" tracking), as shown in fig. 3-A. Subtracting these tracking curves yielded the vessel diameter distension waveform, as displayed for the 4% arterial distension in fig.3-B (gray curve). An excellent match with the distension curve directly derived from the FSI simulations (black curve) was achieved (for all three cases). For the three simulated degrees of distension, the distension waveform obtained from the FSI-US coupling procedure is shown for the inner and outer wall tracking in Fig. 3-C & D.

In fig. 4, we further analyzed arterial distension using the circumferential strain $\Delta D/D$, which is frequently used in clinical practice as a measure of arterial distensibility. Using the simulated RF-data, the circumferential strain $\Delta D/D$ was computed at several depths within the wall for all three distension degrees, as indicated by the dashed lines in fig. 4. Assuming an incompressible material and neglecting deformation along the vessel axis, the theoretical $\Delta D/D$- curves were also computed

17

and indicated by the solid lines. While the circumferential strain $\Delta D/D$ obtained from theoretical calculation as well as FSI computations resulted in a $1/D^2$ -relationship, this was not the case for the wall tracking based on the FSI-US coupling procedure.

415   Interestingly, there was a very good match between theory and ultrasound wall tracking based on the FSI-US data of the inner and outer wall tracking. However, tracking based on points within the vessel wall resulted in an S-shaped relationship between $\Delta D/D$ and depth in the arterial wall.

B.Flow imaging application: measurement of wall shear rate

420   Fig. 5 shows the two-dimensional velocity (angle-corrected values) and derived shear rate distribution in depth and time, obtained from the FSI-US coupling procedure for the three simulated cases. Since mass flow inlet boundary conditions were applied, smaller distensions resulted in higher velocities and shear rate profiles. For all cases, FSI-US shear rate reaches its maximum value at a certain distance from the wall. Fig.

425   6 shows in more detail the correspondence between the ground truth information (velocity profile and shear rate obtained from the FSI data) and the simulated ultrasound measurements, in case of the largest distension and for two different cardiac frames (as indicated on the velocity curve imposed at the tube inlet). FSI-US derived maximal shear rate is systematically lower than the reference value derived

430   from the FSI simulations, with the largest discrepancy appearing near peak systole. This is also demonstrated in the upper panels of fig. 7 showing the maximal shear rate curve throughout the cardiac cycle for the three simulated cases. The lower panels of fig. 7 reveal the position of the maximal shear rate in the cardiac cycle as obtained from the FSI-US data, compared to the actual wall position. There was no

435   clear relation between the location of maximal shear rate and the actual position of the arterial wall. However, one can notice that the position of the ultrasound-derived

maximal shear rate shows an asymmetrical trend compared to the vessel centre: maximal shear rate is measured closer to the posterior wall than to the anterior wall for all distension degrees (see also figure 7). For the anterior wall, the average distance between the position of maximal shear rate and the wall was 0.747±0.119, 0.815±0.185 and 0.810±0.138 mm for the 1%, 4% and 9% distension case, respectively. For the posterior wall, values were 0.626±0.119, 0.647±0.138 and 0.689±0.155 mm.

Despite the fact that the maximal shear rate obtained from FSI-US is lower than the maximal FSI values, it is clear from fig. 7 that both values show similar patterns throughout the cardiac cycle and that they are correlated. To assess whether this correlation is the same for the three simulated cases, the shear rate values obtained from FSI-US simulations are plotted versus the FSI ground truth values in figure 8. Both curves were aligned in time (using the peak as reference) to account for the temporal filtering effect resulting from the averaging and smoothing operations on the FSI-US velocity curves. Ultrasound significantly underestimated the actual wall shear rate for all three distension degrees but the same linear trend was observed for the different cases ($y=0.44x+65$ 1/s). It is clear that the underestimation by ultrasound augments for increasing shear rate values. For an FSI reference value of 200 1/s, the underestimation is about 25%, increasing to about 50% for a reference value of 800 1/s.

Discussion

The work presented in this study is an extension of our previously described method of coupling CFD and Field II ultrasound simulations, allowing us retrieving RF-signals from complex flow fields with flexible control of flow and imaging parameters [3]. Using this tool, different uni- and multidimensional flow imaging methods were evaluated in the presence of complex flow [6]. However, this simulation tool was based on flow simulations assuming rigid walls, neither did it allow us to derive RF-data from the vessel wall itself. Therefore, we extended our approach and coupled the Field II ultrasound simulation software with flow and tissue data obtained from FSI-simulations, which take into account the complex interaction between fluid and arterial wall mechanics when solving the flow and structural equations. As for the CFD-US simulation environment, RF-signals were simulated with the Field II ultrasound software where tissue is represented by point scatterers. Scatterer positions were derived from the fluid velocity and structural displacement fields as computed by an in-house FSI-code ("Tango") which allows to couple Fluent with Abaqus. To validate the coupling procedure (in particular the computation of the fluid and structure scatterer phantom) and to demonstrate the potential of the multi-physics model, we simulated the flow in a deforming straight 3D tube with dimensions and fluid characteristics representative for blood flow in the common carotid artery. Three different degrees of arterial distension were modeled and the potential of the simulation tool was demonstrated with ultrasonic distension and wall shear rate measurements.

Integration of biomechanics and ultrasonic analysis is not novel, but in most studies either the biomechanical part has been simplified (using analytical equations or in-

vivo measurements for the flow and/or mechanical behaviour [22-24]), either the ultrasound physics model has been compromised [25]. The work showing the closest agreement with ours was recently published by Balocco et al[26], who proposed a simulation model where the Field II simulation software is integrated with fluid-structure interaction as computed by COMSOL multiphysics. The simulated RF-lines were further processed to produce B-mode, M-mode images, and Doppler blood velocity estimations. Our study extends on our previous CFD-based model, and we elaborate on the scatterer phantom creation and in particular the difficulties related to the interpolation in time and space of scatterer positions in a deforming geometry, which is a non-trivial problem. As for the fluid-structure interaction simulations, we used an in-house code (Tango) which allows to (strongly) couple any black-box CFD and structural solver (in our case Fluent with Abaqus). The described methodology is therefore generically applicable. We further applied our simulation tool to ultrasonic measurements of hemodynamic (wall shear rate) and mechanical (vessel distension) indices of arterial function. These techniques are commonly applied in pre-clinical vascular research, but there is still a lack of clarity concerning the accuracy (shear rate) and the link with intrinsic mechanical properties (vessel distension) hampering their use on a larger scale in clinical studies. Multiphysics models as presented here and by Balocco et al. will allow us to ultimately reveal the effectiveness and reliability of these imaging modalities.

Although a validation of our model in a strict sense is not straightforward, our results clearly indicate that our approach provides RF-data leading to realistic ultrasound images (as we also previously demonstrated for the CFD-US simulations[27]). For the vessel wall imaging, the distension curve as obtained by tracking Abaqus nodes from the FSI-simulation was compared to the ultrasonic wall tracking result at a similar

depth in the vessel wall (fig. 3). This was shown in fig.3-B for the 4%-distension case with a quasi perfect match between input and output of the FSI-US coupling procedure, and a similar level of agreement was obtained for the two other cases. The fluid phantom used for the FSI-US integration resulted in velocity profiles showing a clear resemblance with the Fluent solution (fig.6), and demonstrating typical deviations from the actual velocity profile (especially near the wall) as can be expected from ultrasound measurements. Data are also in good quantitative as well as qualitative agreement with in vivo data reported by Hoeks et al. and Brands et al[9, 20].

We subsequently focused on two applications of clinically relevant vascular imaging methods, one involving the arterial wall and one involving the blood flow. A commonly applied measure for arterial distensibility is $\Delta D/D$ (= circumferential strain in case of planar deformation). Ultrasonic wall tracking algorithms have been developed to track vessel wall motion based on integrating estimated tissue velocities[2]. The RF wall tracking based on our FSI-simulations demonstrated that $\Delta D/D$ is very sensitive to measurement location (cfr. fig. 4), with a decreasing trend in $\Delta D/D$ from inner to outer wall , confirming results from previous in-vivo studies[7]. Although we expected a $1/D^2$ dependency on theoretical grounds, we rather obtained an S-curve of $\Delta D/D$, which was flattened in the neighborhood of tissue transitions. This curve flattening can be explained by the strong (specular) reflections present near the vessel wall boundaries, which blur the velocity measurement in its immediate neighborhood. Indeed, when repeating the ultrasound simulations without specular reflections, the theoretical $1/D^2$ dependency was obtained (data not shown). Hence, deducing deformation trends and material properties of the studied vessel wall tissue based solely on wall tracking measurements within the arterial wall may

lead to flawed interpretations. This might particularly be the case in the presence of
arterial calcifications, causing sharp echographic interfaces in the arterial wall.

Considering the flow field application, simulation of wall shear rate assessment prevailed excellent agreement with the findings of Brands et al [9, 20], who demonstrated that the maximum of ultrasound-derived wall shear rate was obtained at a certain distance from the wall. We could not observe a relation in the location of maximal shear rate and vessel distension, but maximal shear rate location was closer to the posterior than anterior wall, when calculating the average distance between the vessel wall and maximal shear rate location. The observed distances were in the same order as can be derived from the data shown in Brands et al[9] (± 833μm when deriving this from their reported figures). The (small) difference between FSI-US velocity measurements at the anterior and posterior wall is related to the ultrasound physics (e.g. point spread function of the ultrasound system is asymmetrical in the depth direction with higher intensities below than above the imaged point) and not to the numerical FSI calculations, which show axial symmetry in the results.

Brands et al tested their wall shear rate measurements in-vivo and in-vitro. For 30 in-vivo carotid examinations, they found a low variance on the reproducibility of the wall shear rate measurement (5%)[9]. The in-vitro study entailed validation with laser Doppler anemometry (LDA) in a flow model of a distensible tube. However, a larger discrepancy of 11 % was reported between both methods[9]. Note that LDA has a similar limitation as ultrasound in the sense that it does not allow measurement of flow velocities near a moving wall. Hence, this in-vitro validation does not act as a real reference value for the actual shear rate. It is here that our FSI-US model has an added value. In Figure 8, we have plotted the maximal shear rates as estimated by ultrasound versus the FSI ground truth values. Interestingly, a similar linear relation

was revealed for all distension degrees, suggesting that the underestimation by ultrasound could be compensated for (at least for the simulated setting). It is important to stress that in our analysis, we compare the peak values of the FSI-US and the FSI shear rate, and these do not occur at the same locations. When considering their relationship at the same positions in depth, a better quantitative agreement is obtained especially near the posterior wall. This is illustrated in fig.6: when comparing the FSI-value at the same location as where the ultrasound-derived value reaches its peak (indicated by the ellipse), the numerical values of shear rate are close. This is in line with the experimental validation results of Brands et al[9], who compared ultrasound- and LDA-derived values at the same measuring position Finally, it is worth mentioning that in pulsatile flow conditions, the maximal shear rate not necessarily occurs at the position of the wall itself even for the simple case of a straight tube (as illustrated by Figure 6).

Note, however, that further optimization of the simulation of shear rate imaging is necessary before drawing hard conclusions with respect to real-life in vivo applications. In particular, the ultrasound signal generated by the wall should be taken into account as well as an extensive study of the influence on the applied clutter filter, which was neglected in this study. Also, the settings applied during processing of the ultrasound data (e.g. temporal and spatial filtering) are crucial for the estimates of velocity and even more for the obtained values of the wall shear rate. As such, the simulations should be well matched with the settings used for the in-vivo imaging. Further, the simulated cases here represent blood flow in straight arterial segments, with a fully developed symmetrical inflow velocity profile. It can be anticipated that in bended arteries and in the vicinity of complex bifurcations (such as the carotid artery), the flow profile will be far more complex. In these conditions, the

correspondence between ultrasound-based estimates of wall shear rate and their actual values will, without any doubt, be far more complex.

Although the multiphysics model as presented in this study represents a major improvement over our existing model, limitations are still present, both at the biomechanical and acoustical level. Concerning the FSI-simulations, different distension degrees could have been modeled by applying stiffer material properties. However, since we were only interested in wall movement and not wall stresses, we only scaled the pressure wave. More realistic material behavior including anisotropic and hyperelastic material properties could have been modeled (at the expense of higher computational times). The influence of the surrounding tissue on the vessel wall movement, residual stresses and effects of longitudinal pre-stretch of the structure could be taken into account in future work. Further, the boundary conditions to solve the fluid problem could be refined by applying a physiologically realistic vascular impedance as outlet boundary condition, inducing more realistic wave propagation phenomena in the tube.

The Field II method is also based on some assumptions: nonlinear propagation of ultrasound waves and multiple scattering are not included, with the latter one limiting the accuracy of distension measurements in-vivo. The Field II-approach also ignores the shape of the scatterers (disc shaped red blood cells). We did not include frequency dependent scattering or noise in our simulations. Furthermore, the tissue echogenic properties are simulated as a combination of random scatters in the wall and mimicked specular reflections along the inner and outer boundary of the wall. Although this results in realistically looking RF spectra, further fine-tuning and optimization towards RF-spectra of actual tissue may be mandatory, especially when simulating more complex arterial tissues with the inclusion of vessel inhomogeneities

and plaque. In particular, the fibrous structure of the vessel wall which leads to

610   scattering correlation in the fiber direction could be included in the phantom modeling.

It should also be stressed that the distension data are solely based on RF-signals

from the wall, while the shear rate application relied only on RF-signals from the flow.

The shown applications should therefore mainly be considered as a demonstration of

the potential of the simulation tool in developing vascular imaging tools, rather than a

615   thorough validation of each of these applications. It is, for that matter, most likely that

the imaging and signal processing setups can be further optimized for each specific

application.

In summary, we demonstrated a simulation environment to validate and develop

ultrasonic vascular imaging applications. An elaborate technique to integrate fluid-

620   structure interaction (FSI) and the Field II ultrasound simulation software was

presented. This multiphysics ultrasound simulation environment was applied to two

ultrasound imaging applications where distensible ultrasound phantoms are

indispensable for their analysis: wall distension and wall shear rate measurement,

applied to the case of a straight 3D tube subjected to three levels of distension. The

625   RF wall tracking algorithm was able to quasi perfectly track the motion of the inner

and outer vessel wall. As anticipated, distension measurements showed a high

sensitivity to measurement location in the wall but the simulations also revealed that

strong specular reflections from tissue transitions potentially cloud correct

measurements within the media of the vascular wall. Further, the flow imaging

630   application revealed that maximal shear rate was measured at a certain distance

from the vessel wall as previously demonstrated in vivo by Brands et al[9, 20] and that

the location where measured shear rate is maximal, is closer to the posterior than to

anterior wall. For the three simulated cases, a similar linear trend between ultrasound

estimated shear rate and the FSI-ground truth was found, suggesting that the

635 underestimated ultrasound values could be corrected for. Based on the above

observations, we conclude that our method to couple fluid-structure interaction and

ultrasound simulations provides realistic radio-frequent signals from both the tissue

and the blood pool which can be processed into ultrasound-derived medical images

and measurements. Further research will focus on applications for the ultrasonic

640 investigation of the carotid bifurcation.

645

650

655

ACKNOWLEDGMENTS

665

TABLES

Table 1: Simulation setup for respectively the flow (F) and wall (W) application

Ultrasound set-up parameters for the shear rate and wall distension application		
	Blood flow	Wall distension
f_0=centre frequency	5 MHz	8 MHz
# elements	192	192
Pitch	246µm	203 µm
Height	6 mm	3.25 mm
Focus	2 cm	2 cm
Dynamic receive focusing	Yes	Yes
Expanding aperture	Yes	Yes
Excitation	Sinusoidal	Sinusoidal
Pulseperiods	4	1.5
PRF_{max}	8000 Hz	8000 Hz
PRF	8000 Hz	1000 Hz
Packetsize	64	3
Assigned scatterer properties		
	Mean amplitude	STD
Inner wall (~specular reflections)	0	1
Outer wall (~specular reflections)	0	0.01
Wall	50	0.01
Blood	100	0.01

670

FIGURE LEGENDS

Figure 1: _Panel A:_ Illustration of the principles behind the creation of the fluid scatterer phantom. In case of distensible fluid geometries, absolute positions can not be compared between two time steps and hence linear interpolation of the velocity fields is not straightforward. Instead, the velocity field at the future timestep $T_{2,FSI}$ is used to derive the scatterer displacement. Scatterers are mapped in space to the next timestep using the fluid grid displacement and hence the same relative position of the scatterer in the vessel is obtained. Once the future position of the concerned scatterer is determined, the velocity vector is extracted. Using these future velocity vectors, the scatterers will follow the vessel wall motion. This is illustrated in case of an increasing and decreasing fluid volume. In the latter case, the same absolute position of the red point at $T_{FSI,1}$ is a point outside the fluid volume. In the former case the red point ends up too far from the vessel wall, indicating the need for mapping scatterer positions conserving the relative position in the vessel wall. _Panel B:_ A flowchart of the creation of the fluid phantom

Figure 2: Illustration of the principles behind the creation of the structure scatterer phantom. The vessel wall is divided in several layers using hexahedral elements, allowing flexibility in changing scattering properties according to the concerned vessel layer. Due to the complex composition of the vessel wall (potentially including calcifications etc…), scatterers were created in the individual hexahedrons. A random uniform spatial distribution was obtained by creating them in a bounding box and deleting scatterers outside the considered hexahedron. Besides these random scatterers, specular reflections created by tissue transition regions were mimicked by placing scatterers at fixed distances at the wet and dry side of the structure.

Figure 3: M-mode images were created based on RF-data obtained from the FSI-US coupling procedure, for the three simulated degrees of distension. These were further used for tracking the vessel wall motion using a modified autocorrelation approach[2]. Panel A shows an RF M-mode image for the 4% distension case. Inner and outer wall tracking are shown for all cases in panels C and D. Panel B shows the comparison between the ultrasound wall tracking and the ground truth obtained from tracking Abaqus nodes.

Figure 4: The circumferential strain $\Delta D/D$ for all distension degrees obtained with the FSI-US coupling procedure (dashed lines) and compared to the theoretical relationship (solid lines).

Figure 5: The two-dimensional velocity and shear rate distribution in depth and time for all degrees of distension.

Figure 6: The velocity and shear rate profiles obtained from the FSI-US coupling procedure (gray) are compared to the FSI ground truth (black) at 2 cardiac frames, as indicated on the velocity curve imposed at the tube inlet. The ellipse indicates the posterior wall has a better agreement of FSI-US and FSI shear rates in space, compared to the anterior wall.
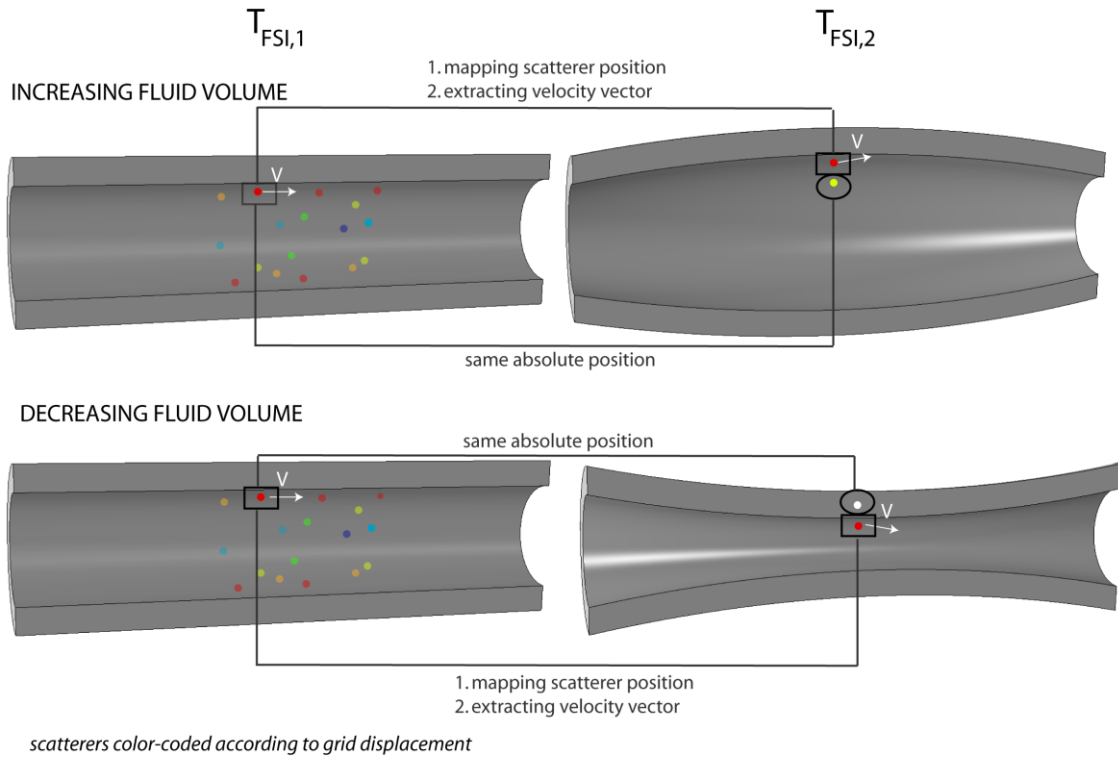
Figure 7: The upper panels show, for the 3 degrees of distension, the maximal shear rate throughout the cardiac cycle as derived from the FSI-data and from the FSI-US simulations. The lower panels show the position of the maximal shear rate compared to the actual wall position. The average distance of the maximal shear rate to the wall position is given for the anterior and posterior side.

31

Figure 8: Correlation between the maximal shear rate as estimated by ultrasound and the FSI ground truth values for all distension degrees. For the three simulated cases, a similar linear trend is found (y = 0.44 x + 65 1/s).
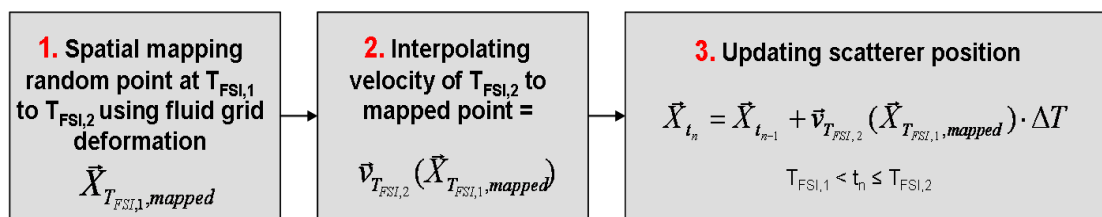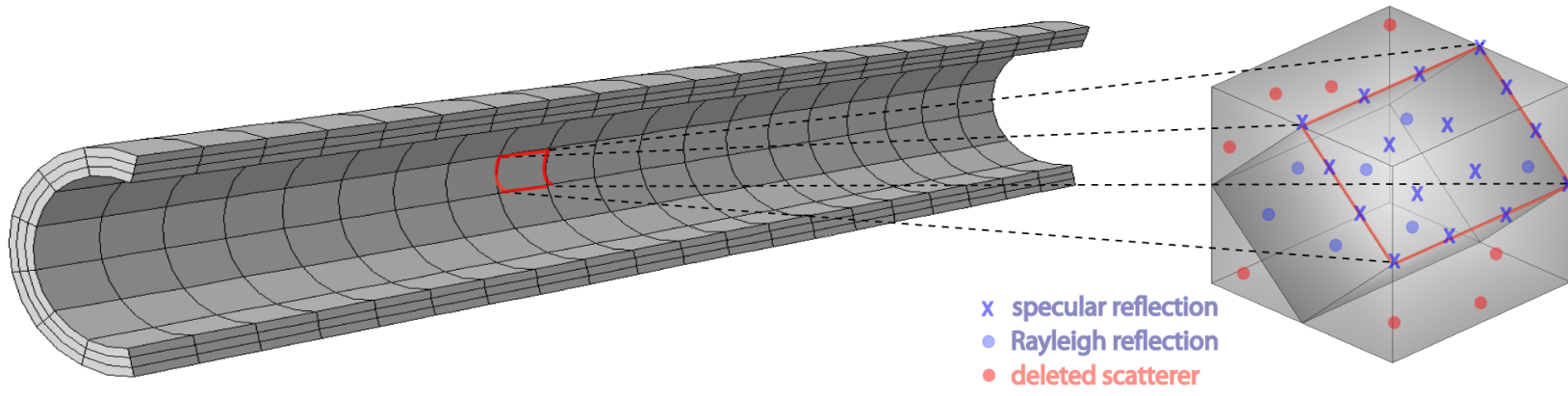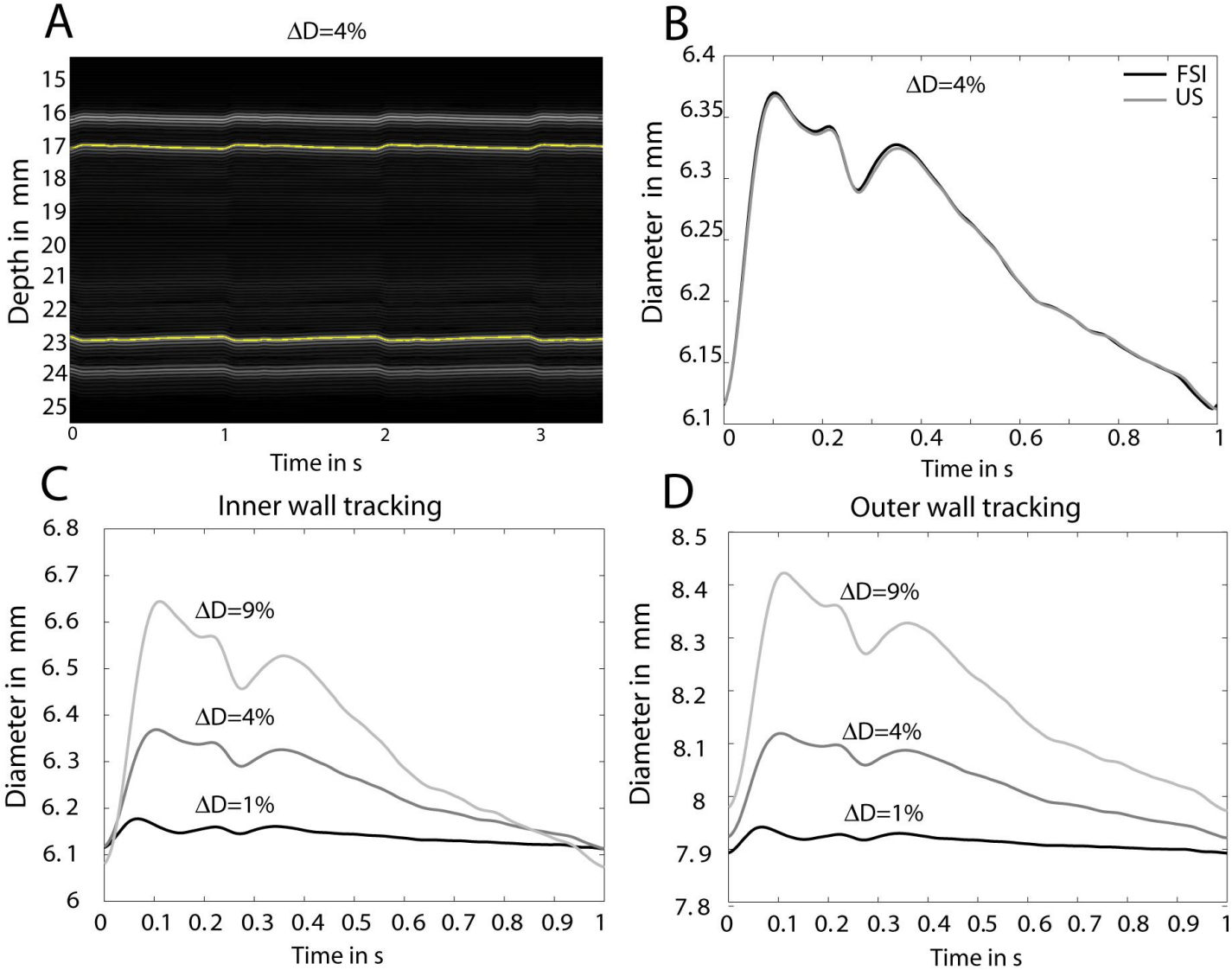
FIGURES

Figure 1

A

$T_{FSI,1}$ $T_{FSI,2}$

INCREASING FLUID VOLUME

1. mapping scatterer position
2. extracting velocity vector

same absolute position

DECREASING FLUID VOLUME

same absolute position

1. mapping scatterer position
2. extracting velocity vector

scatterers color-coded according to grid displacement

B

1. Spatial mapping random point at $T_{FSI,1}$ to $T_{FSI,2}$ using fluid grid deformation

$$\vec{X}_{T_{FSI,1},mapped}$$

2. Interpolating velocity of $T_{FSI,2}$ to mapped point =

$$\vec{v}_{T_{FSI,2}}(\vec{X}_{T_{FSI,1},mapped})$$

3. Updating scatterer position

$$\vec{X}_{t_n} = \vec{X}_{t_{n-1}} + \vec{v}_{T_{FSI,2}}(\vec{X}_{T_{FSI,1},mapped}) \cdot \Delta T$$

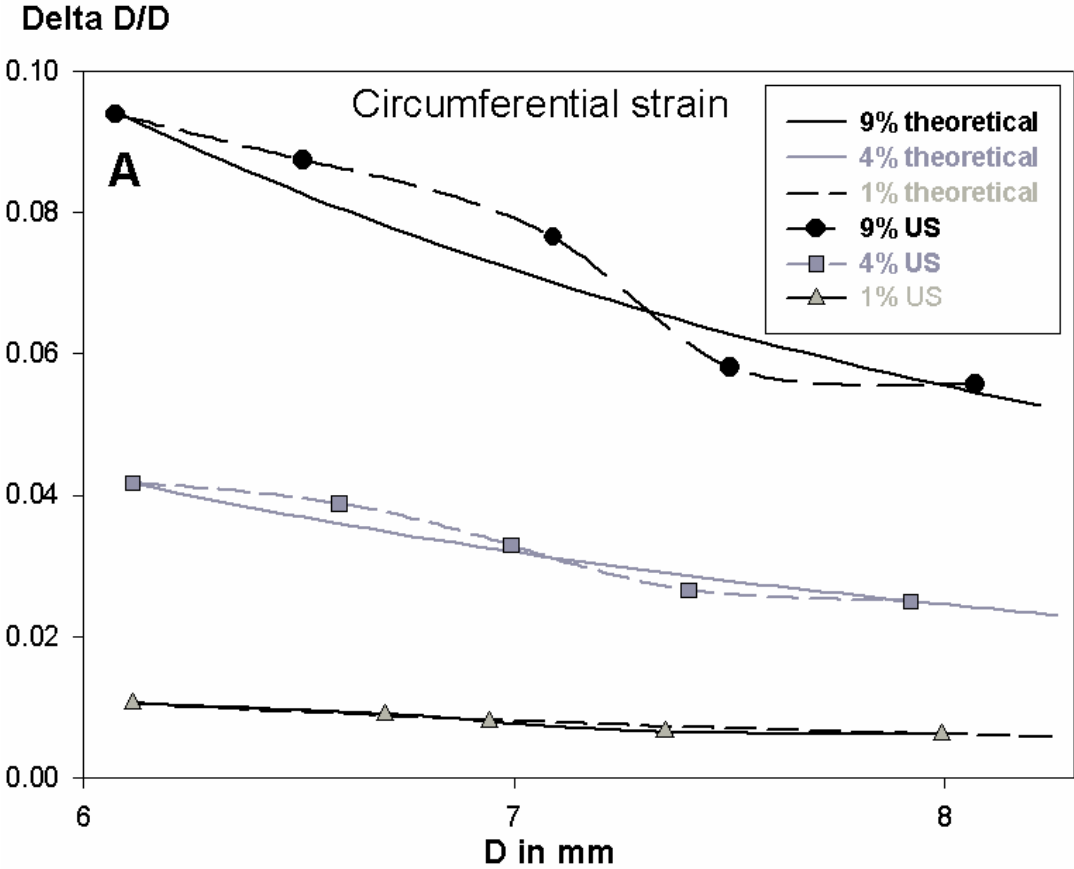$$T_{FSI,1} < t_n \leq T_{FSI,2}$$

Figure 2

x   specular reflection
●   Rayleigh reflection
●   deleted scatterer

Figure 3

Figure 4

Figure 5

VELOCITY

SHEAR RATE

Figure 6

$\Delta D = 9\ \%$

Figure 7

Figure 8

Shear rate in 1/s: US versus FSI
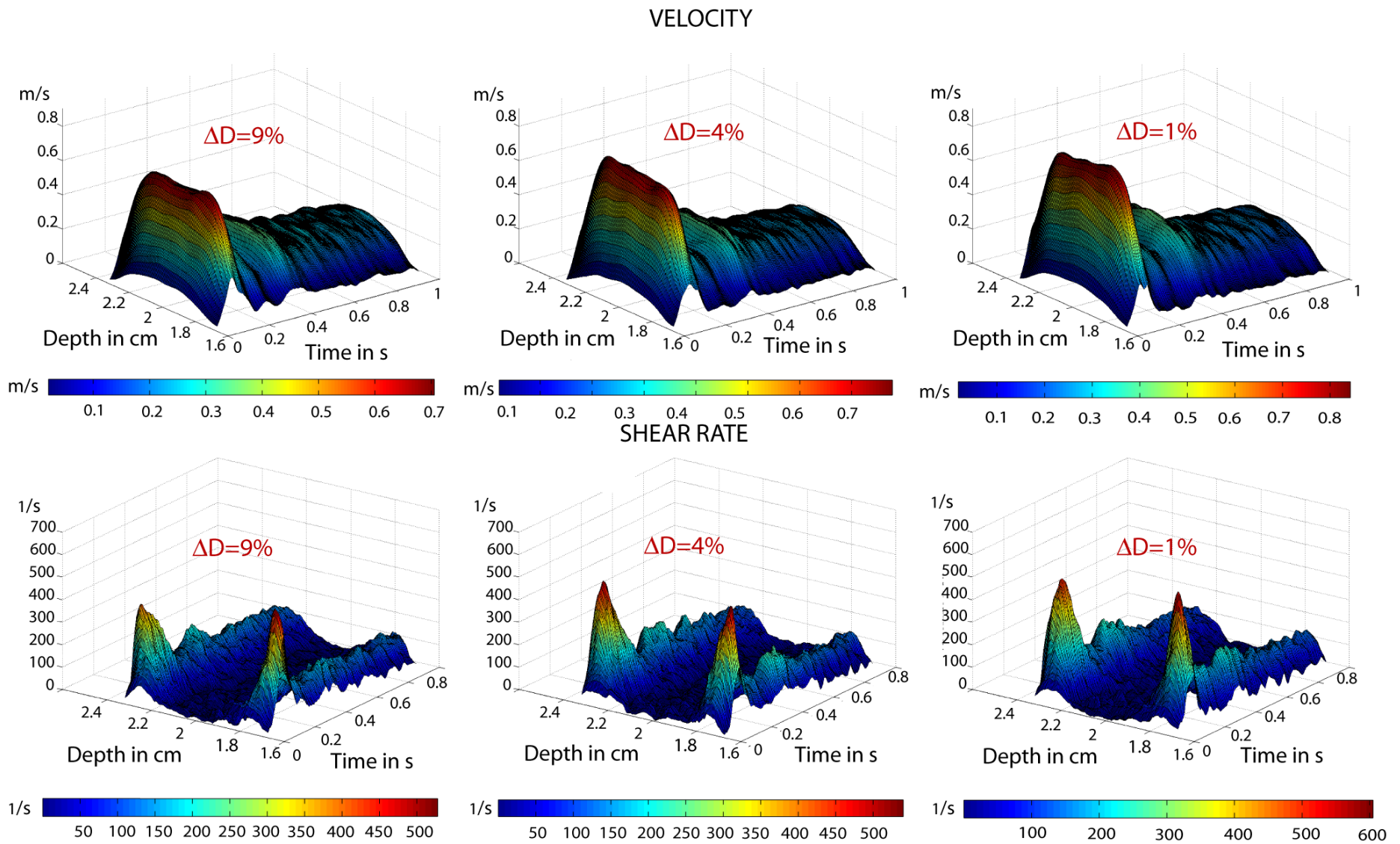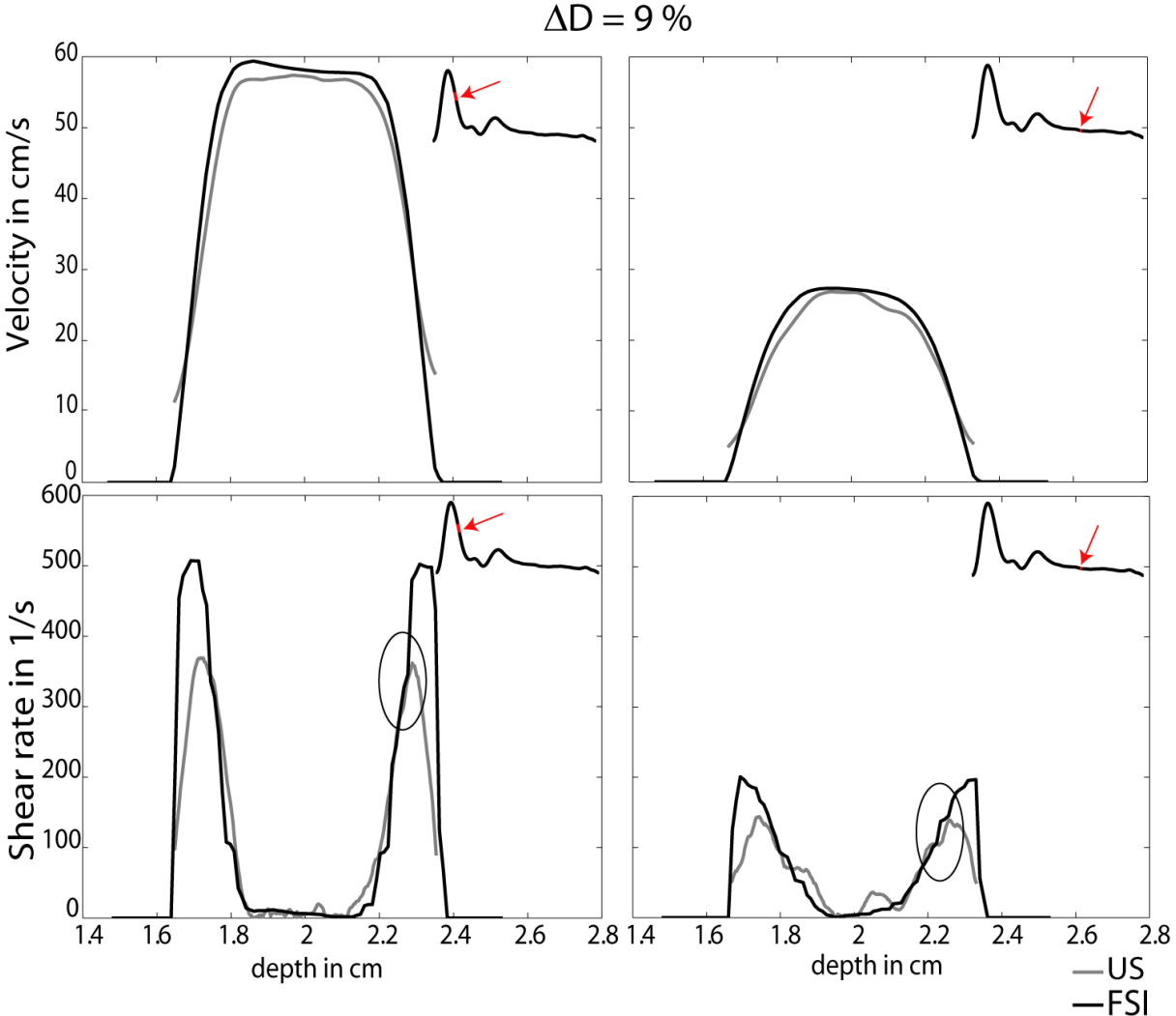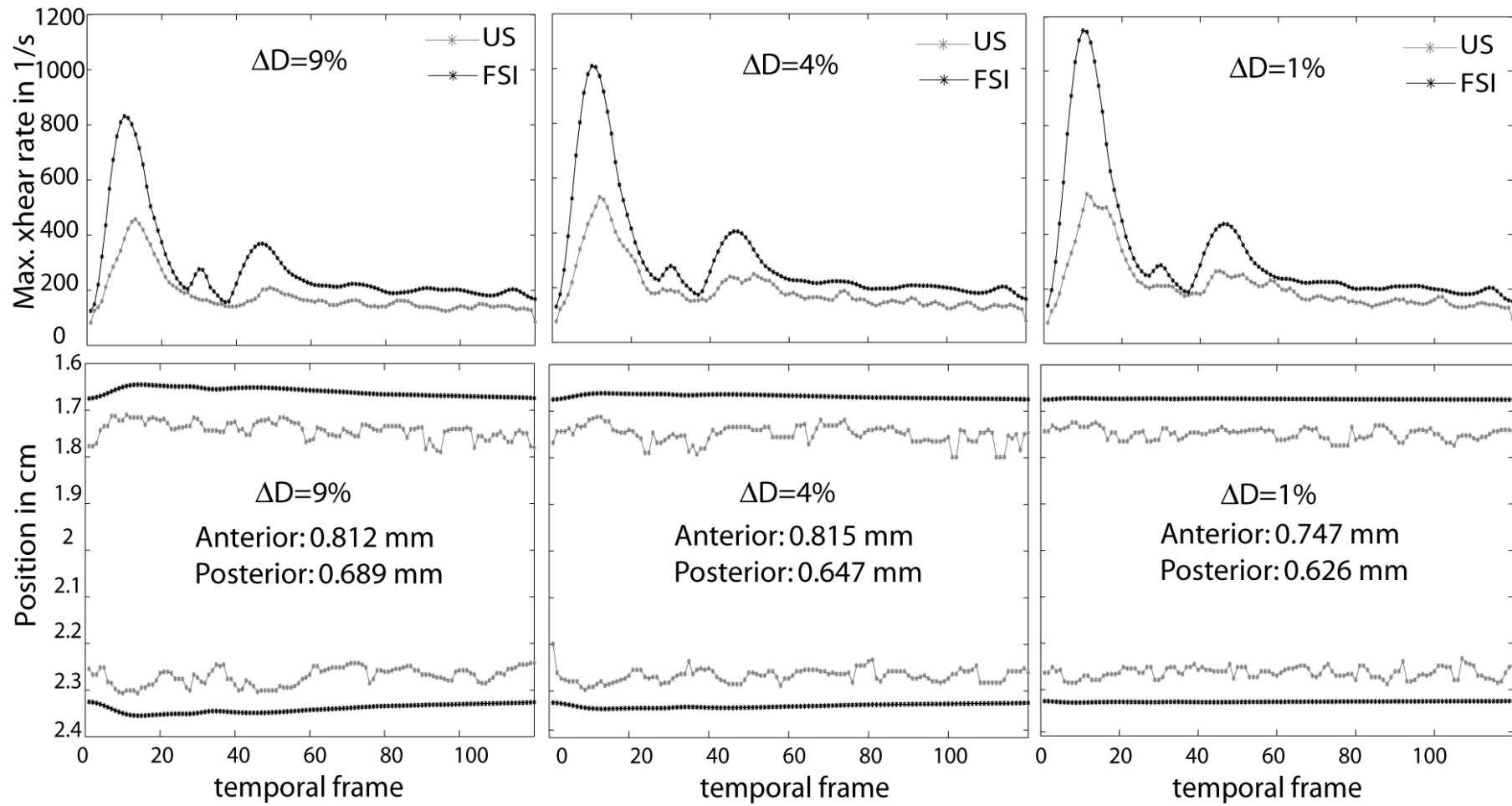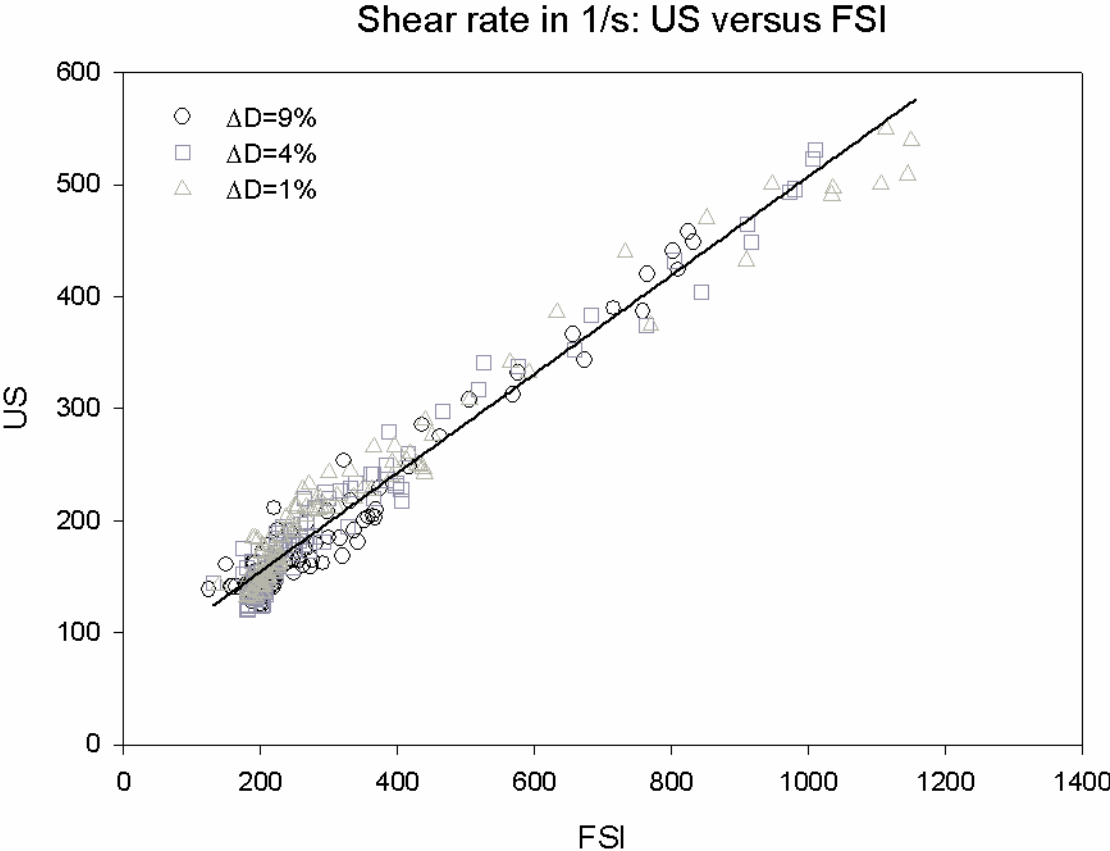
REFERENCES

1. D. A. Steinman, J. B. Thomas, H. M. Ladak, J. S. Milner, B. K.Rutt and J. D. Spence, "Reconstruction of carotid bifurcation hemodynamics and wall thickness using computational fluid dynamics and MRI," Magn. Reson. Med. **47**, 149-159 (2002).
2. S. I. Rabben, S. Bjaerum, V. Sorhus and H. Torp, "Ultrasound based vessel wall tracking: an autocorrelation technique with RF center frequency estimation," Ultrasound in Med. & Biol. **28**, 507-517 (2002).
3. A. Swillens, L. Lovstakken, J. Kips, H. Torp and P. Segers, "Ultrasound Simulation of Complex Flow Velocity Fields Based on Computational Fluid Dynamics," IEEE TUFFC **56**, 546-556 (2009).
4. J. A. Jensen and N.B.Svendsen, "Calculation of pressure fields from arbitrarily shaped, apodized, and excited ultrasound transducers," IEEE TUFFC **39**, 262-267 (1992).
5. J. A. Jensen, "Field: A program for simulating ultrasound systems," Med. Biol. Eng. Comput. **34**, 351-353 (1996).
6. A. Swillens, P. Segers, H. Torp and L. Lovstakken, "Two-dimensional blood velocity estimation with ultrasound: speckle tracking versus crossed-beam vector Doppler simulations," IEEE TUFFC (in press).
7. P. Segers, S. I. Rabben, J. D. Backer, J. D. Sutter, T. Gillebert, L. V. Bortel and P. Verdonck, "Functional analysis of the common carotid artery: relative distension differences over the vessel wall measured in vivo.," J Hypertension **22**, 973-981 (2004).
8. S. Glagov, C. Zarins, D. P. Giddens and D. N. Ku, "Hemodynamics and atherosclerosis," Arch. Pathol. Lab. Med. **112**, 1018-1031 (1988).
9. P. J. Brands, A. P. G. Hoeks, L. Hofstra and R. S. Reneman, "A non-invasive method to estimate wall shear rate using ultrasound," Ultrasound in Med. & Biol. **21**, 171-185 (1994).
10. P. Causin, J. Gerbeau and F. Nobile, "Added-mass effect in the design of partitioned algorithms for fluid-structure problems," Computer Methods in Applied Mechanics and Engineering **194**, 4506–4527 (2005).
11. J. Degroote, P. Bruggeman, R. Haelterman and J. Vierendeels, "Stability of a coupling technique for partitioned solvers in FSI applications," Computers & Structures **86**, 2224–2234 (2008).
12. J. Degroote, K. J. Bathe and J.Vierendeels, "Performance of a new partitioned procedure versus a monolithic procedure in fluid-structure interaction.," Computers & Structures **87**, 793–801 (2009).
13. J. Vierendeels, L. Lanoye, J. Degroote and P. Verdonck, "Implicit coupling of partitioned fluid-structure interaction problems with reduced order models," Computers and Structures **85**, 970-976 (2007).
14. H. M. Hilber, T. J. R. Hughes and R. L. Taylor, "Improved numerical dissipation for time integration algorithmsin structural dynamics," Earthquake Eng. and Struct. Dynamics **5**, 283–292 (1977).
15. G. E. Tupholme, "Generation of acoustic pulses by baffled plane pistons," Mathematika **16**, 209–224 (1969).
16. P. R. Stepanishen, "Transient radiation from pistons in an infinite planar baffle," J. Acoust. Soc. Am. **49**, 1629–1638 (1971).
17. J. M. Thijssen, "Ultrasonic speckle formation, analysis and processing applied to tissue characterization," Pattern Recognit. Lett. **24**, 659–675 (2003).
18. P. L. Tallec and J. Mouro, "Fluid structure interaction with large structural displacements," Comput. Methods Applied Mech Engineering **190**, 3039-3067 (2001).
19. M. A. Fernandez and P. L. Tallec, "Linear stability analysis in fluid–structure interaction with transpiration. Part I: Formulation and mathematical analysis," Comput. Methods Applied Mech Engineering **192**, 4805–4835 (2003).

20. A. P. G. Hoeks, S. K. Samijo, P. J. Brands and R. S. Reneman, "Noninvasive Determination of Shear-Rate Distribution Across the Arterial Lumen," Hypertension **26** (1995).
21. C. Kasai, K. Namekawa, A. Koyano and R. Omoto, "Real-time twodimensional blood flow imaging using an autocorrelation technique," IEEE Trans. Sonics Ultrason. **32**, 458–463 (1985).
22. J. A. Jensen and P. Munk, "Computer phantoms for simulating ultrasound b-mode and cfm images," Acoust. Imag **23** (1997).
23. M. Schlaikjer, S. Torp-Pedersen and J. A. Jensen, "Simulation of RF data with tissue motion for optimizing stationary echo canceling filters," Ultrasonics **41**, 415-419 (2003).
24. A. T. Kerr and J.W.Hunt, "A method for computer simulation of ultrasound doppler color flow images—I. Theory and numerical method," Ultrasound Med. Biol. **18**, 861-872 (1992).
25. M. Khoshniat, M. Thorne, T. Poepping, S. Hirji, D. Holdsworth and D. Steinman, "Real-time numerical simulation of Doppler ultrasound in the presence of nonaxial flow," Ultrasound in Med. & Biol. **31**, 519-528 (2005).
26. S. Balocco, O. Basset, J. Azencot, P. Tortoli and C. Cachard, "3D dynamic model of healthy and pathologic arteries for ultrasound technique evaluation," Medical Physics **35**, 5440-5450 (2008).
27. A. Swillens, T. D. Schryver, L. Lovstakken, H. Torp and P. Segers, "Assessment of Numerical Simulation Strategies for Ultrasonic Color Blood Flow Imaging, Based on a Computer and Experimental Model of the Carotid Artery," Annals of Biomedical Engineering **37**, 2188 (2009).